Azimuthal Anisotropy of Charged Particles in Pb+Pb Collisions with ATLAS Detector

Xiaoning Wang

Advisor: Anne Sickles

University of Illinois at Urbana-Champaign

(Dated: April 8, 2021)

The quark gluon plasma (QGP) produced in the ultra-relativistic heavy-ion collisions is a novel state of matter where color charged particles are deconfined at extreme temperature and density. During the collisions, particles from scattering with low momentum transfer, or soft-scattered particles, form the QGP. Evidence shows that the QGP can be modeled with relativistic hydrodynamics of a nearly ideal fluid. The initial shape of QGP is transformed into azimuthal anisotropy in low transverse momentum (p_T) final state particles those originate from the soft-scattering. Event-by-event nucleon position fluctuations create triangular and higher order eccentricities in the QGP shape. Particles from scattering with large momentum transfer, or hard-scattered particles, interact with and experience energy loss to the QGP. Azimuthal anisotropy of high p_T particles those originate from hard-scattering is sensitive to fluctuations in both the QGP shape and the energy loss mechanism. Azimuthal anisotropy analysis can be done using multi-particle cumulant method. The ratio of momentum differential two- to four-particle cumulant of high p_T particles can be used to isolate the energy loss fluctuations from QGP fluctuations. This paper presents an overview of the current theoretical understanding and experimental efforts of the azimuthal anisotropy analysis, then propose for a new measurements using the multi-particle cumulants on high p_T charged particles using ATLAS 2018 data.

I. INTRODUCTION

A. Quark Gluon Plamsa

One of the main purposes of performing the ultra-relativistic heavy-ion collisions, such as those done at the Large Hadron Collider (LHC) and the Relativistic Heavy Ion Collider (RHIC), is to produce a hot, dense nuclear matter at extreme temperature and density. Under normal conditions, color charged particles can only exist in "colorless" bound states known as *hadrons*, for example, protons and neutrons. This is because the strong interaction intensifies at increasing distance and lower energy, a phenomenon known as *asymptotic freedom*. In contrast, with high particle density and temperature present in high energy nucleus collisions, the composite states of particles dissolve into their constituent *partons*— quarks and gluons, giving *quark-gluon plasma* (QGP) [1].

B. Modeling the QGP as A Nearly Ideal Fluid

The current understanding of the heavy-ion collision process can be roughly divided into the following stages [2]. Starting with the nuclear impact, constituent partons those originally move along beam direction scatter off each other and randomize their directions. For most partons, soft scattering happens, meaning relatively low amount of momentum was transferred. This process creates the QGP with an initial geometry, which then undergoes collective expansion due to internal pressure. As the expansion cools down the system, particles in the QGP began to form color neutral bound states of hadrons, which interact with each other, decay and create increasing number of particles with decreasing energy as they fly out to surrounding detectors.

As shown in Fig. 1, the collision geometry of two incoming nuclei gives an elliptical shape, creating pressure gradients that lead to an azimuthal modulation in the particle distribution. This modulation can be characterized by a Fourier decomposition [3],

$$\frac{dN}{d\phi} = \frac{N}{2\pi}\left(1 + 2\sum_{n=1}^{\infty} v_n \cos(n(\phi - \Psi_n))\right) \tag{1}$$

where v_n is the nth order Fourier coefficient and Ψ_n is the nth order participant plane angle.

It has been proposed as early as in the 1950s that the QGP can be described macroscopically as an ideal relativistic fluid [5]. In 2001, for the first time, experimental data from
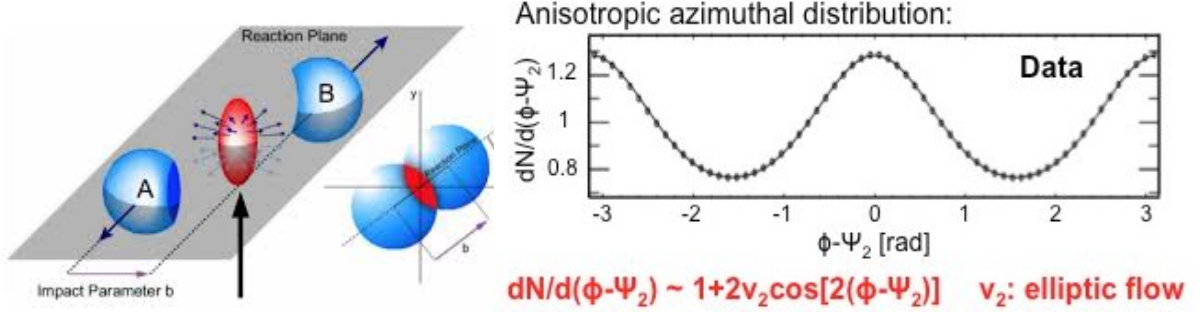
FIG. 1: (left) The geometry of nuclei collision [?] and (right) elliptical azimuthal anisotropy in particle production [4].
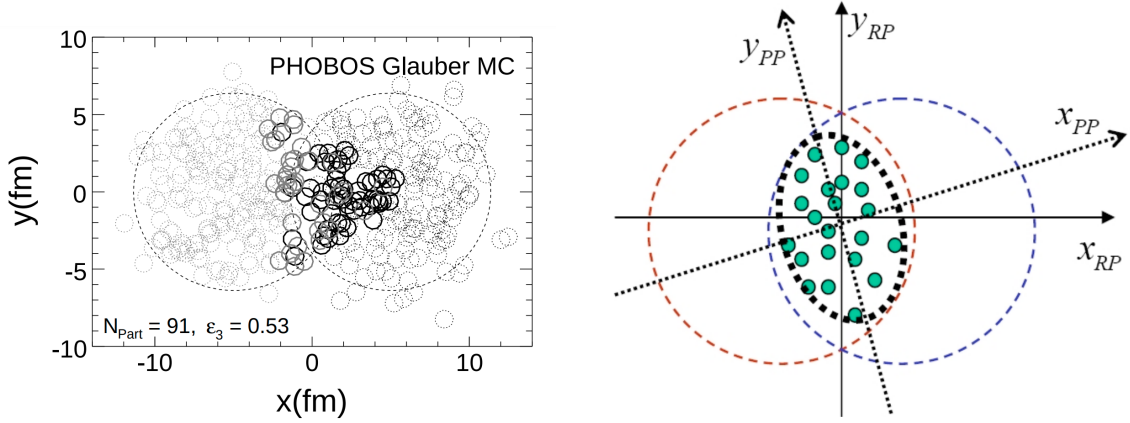

FIG. 2: (left) Simulated nucleon positions [8] and (right) a tilted second order participant plane [9].

34 the Au+Au collisions at the average center of mass energy per nucleon-pair $\sqrt{s_{NN}} = 130$

35 and $\sqrt{s_{NN}} = 200$ GeV at RHIC agreed with predictions using ideal fluid hydrodynamics [6].

36 However, this model diverges from data at larger impact parameters. It was later proposed

37 that the transition to later hadronic stage needs a microscopic modeling, and a small but

38 non-zero viscosity is required for the QGP, motivating for a series of "hybrid models" those

39 combines pre-QGP, post-QGP treatments with viscous hydrodynamics [7].

40 Another key insight is the role of fluctuations in the initial geometry [8]. It can be

41 shown by Monte Carlo simulation that, the nucleons those participate in the collision are

42 not always within the elliptical overlap of two nuclei. Instead, they fluctuate in each collision

43 and can create higher order eccentricities. Shown in the left plot of Fig. 2 is the simulation

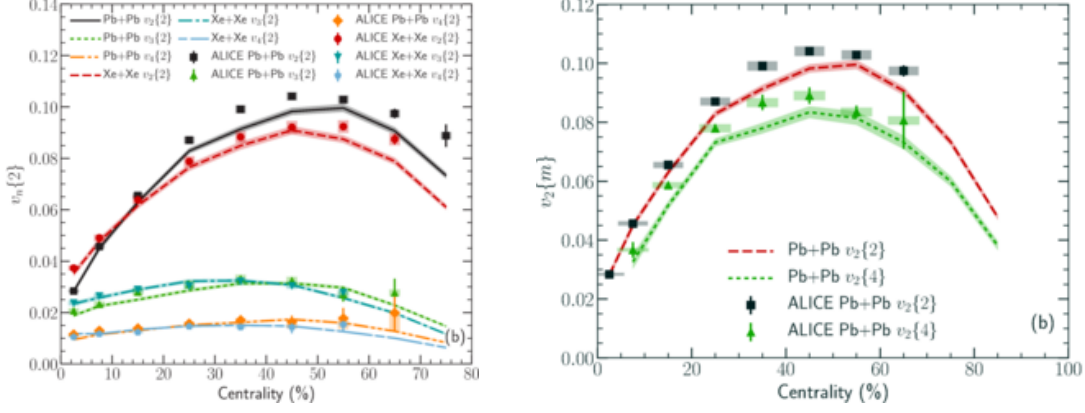44 of a single collision of two nuclei. The nucleons in the two nuclei are shown in gray and

FIG. 3: (left) Low p_T v_n and (right) multi-particle cumulants measured at LHC compared to hybrid viscous hydrodynamical model [10].

45 black. Participant nucleons are indicated as solid circles, while spectators are dotted. This

46 particular collision has created an approximately triangular geometry. On the other hand,

47 the orientation of participant plane (PP) can also deviates from the reaction plane (labelled

48 on the left figure in Fig. 1 for some collisions. An example of a tilted Ψ_2 for a particular

49 collision is shown on the right plot of Fig. 2, where green dots indicate nucleon positions.

50 Current models of event-by-event hybrid models have been successful in explaining the

51 translation of initial QGP geometry into final particle anisotropy in the soft sector [10, 11].

52 For example, shown in Fig. 3 are comparisons between predictions made for v_n and multi-

53 particle cumulants of v_2 (see more discussion on Section III) in different systems at the LHC

54 using a fixed set of model parameters matched to a Au+Au measurement with measured

55 results [10], which achieved an overall good agreement.

56 ### C. High p_T Region: Probe QGP through Parton Energy Loss

57 In the much rarer hard scattering during nucleon-nucleon collision, pairs of back-to-back

58 travelling partons with large transverse momentum (p_T) are produced. Each parton splits

59 more partons which hadronize, forming highly collimated cones of particles, termed *jets* [12].

60 Jet production in proton-proton (pp) collisions at LHC can be described by pertubative

61 QCD (pQCD) calculations. The jet cross-sections at collision center of mass energy $\sqrt{s} =$

62 2.76, 7, 8 and 13 TeV have been measured [13–16]. Shown in the left figure of Fig. 4 are

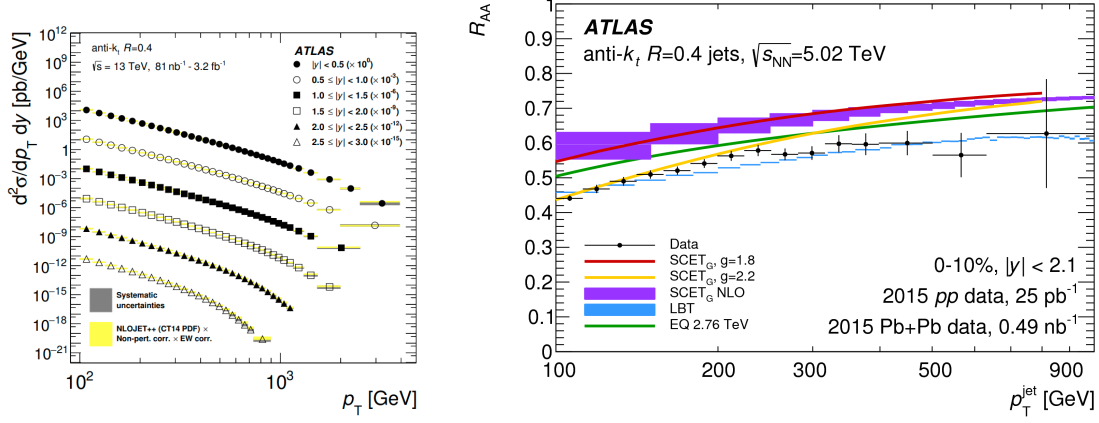63 the measured jet cross section compared to NLO calculations from ATLAS [17] at $\sqrt{s} = 13$

FIG. 4: (left) Comparison of NLO pQCD model calculation NLOJET++ [18] to jet production measurements at ATLAS with different rapidity $|y|$ range [17]. (right) R_{AA} measured at ATLAS comparing to 5 different model calculations [19].

TeV, where measured jet production agrees with theory within uncertainty.

In heavy-ion collisions, hard-scattered partons travel through and interact with the QGP. These fast-travelling partons lose energy to the medium through collisional and induced gluon radiations, a phenomenon known as *jet quenching* [20]. The QGP modification of the jet production [19, 21] and high p_T particles [22–24] those originate from hard-scattered partons in heavy-ion collisions with respect to pp collisions can be described by the *nuclear modification factor R_{AA}*, defined as,

$$R_{AA}(p_T) = \frac{dN_{AA}/dp_T}{\langle N_{coll}\rangle dN_{pp}/dp_T} \tag{2}$$

where N_{AA} and N_{pp} are the jet or charged particle yields in heavy-ion (AA) and pp collisions, and $\langle N_{coll}\rangle$ is the expected number of collisions in heavy-ion collisions as a scale factor. Shown on the right of Fig. 4 are the measured R_{AA} for jets by ATLAS [19]. R_{AA} shown is smaller than 1, indicating jets production is "quenched" in heavy-ion collisions in comparison to pp. The high energy jets probe the QGP at very short length scale. QGP modified hard-scattered products serve as "microscopes" for characterizing the QGP from a tomographical point of view [12].

The distance travelled by a hard-scattered parton in the QGP, and thus its expected energy loss, is dependent on its direction, as shown in the left figure of Fig. 5. Azimuthal anisotropy in high p_T particles are expected to be sensitive to both the energy loss mechanism and the properties of QGP [25, 26]. For exanoke, fluctuations in the QGP initial geometry
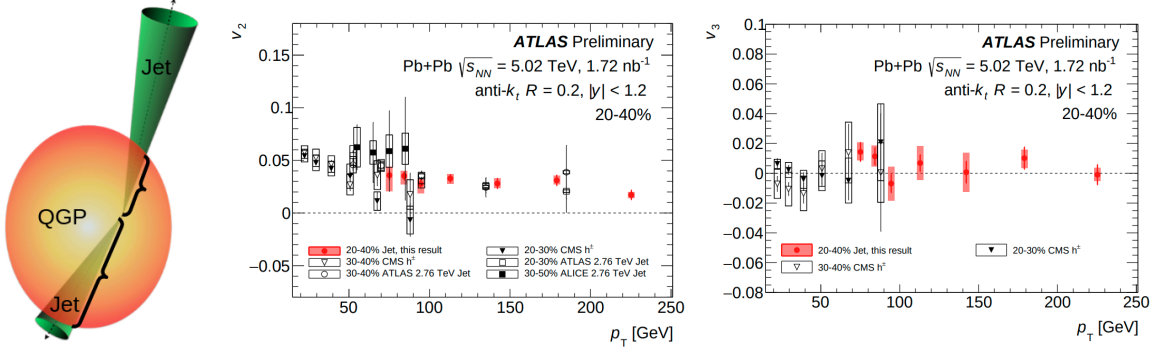
FIG. 5: (left) Different propagation length experienced by jets at different direction, and the measurement of (middle) $v_2(p_T)$ and (right) $v_3(p_T)$ at LHC using jets at $\sqrt{s_{NN}} = 2.76$ TeV by ATLAS [30] and ALICE [29], at $\sqrt{s_{NN}} = 5.02$ TeV with jets by ATLAS [28] and with charged particles (labelled $h^{\pm}$) by CMS [27].

create higher ordered v_n, $n > 2$, in low p_T as shown in Fig. 3, but their role remains unclear in high p_T. Measurements at the LHC using jets and charged particles have shown non-zero v_2, however, v_3 is consistent with zero [27–29] as shown in Fig. 5.

In addition to the propagation length fluctuation created by initial geometry, high-p_T anisotropies are also sensitive to additional fluctuations in the hard sector, including the parton energy loss and jet fragmentation [31] process. Prior to hadronization, the number of re-scattering experienced in the medium by each parton fluctuates, creating fluctuation in energy loss [32]. In experiments, jets are measured by final state particles, and the fragmentation of each parton into final state particles is also a probabilistic process.

To understand the role of fluctuations from these mechanisms, it is important to identify measurables that probe the effect of each process. This paper proposes an anisotropy measurement in the high-p_T region with a particular emphasis to isolate fluctuations of the hard sector from the fluctuations in QGP geometry. The proposed data to use approximately 10 times the statistics of the measurement by CMS [27]. Section II discusses the proposed data source, ATLAS detector at the LHC. Section III explains proposed techniques. Section IV will outline a timeline for the proposed measurement.
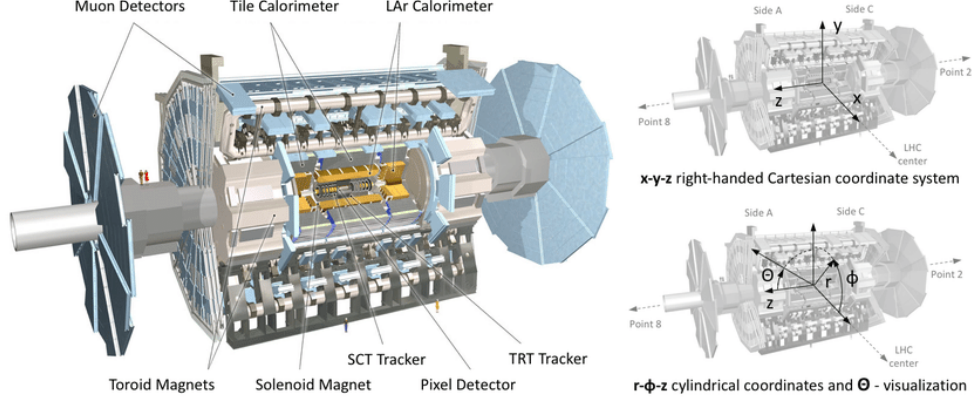
FIG. 6: (left) Schematic view of ATLAS detector and its in Cartesian and cylindrical coordinate system [35].

II. THE LHC AND ATLAS DETECTOR

A. The LHC

The Large Hadron Collider (LHC) underground beneath the France-Switzerland border is the world's highest-energy particle collider built by the European Organization for Nuclear Research (CERN). Installed in a circular 26.7 km tunnel, the LHC consists of two rings with counter-rotating beams of particles [33]. Achieving its first collision at 2010, the LHC has then been operating and being upgraded, with Run 1 taking data between 2009-2013, and Run 2 between 2015-2018. Now the LHC is being further upgraded with the goal of implementing the High-Luminosity Large Hadron Collider (HL-LHC).

B. ATLAS Detector

The ATLAS detector is a multipurpose particle detector installed at the LHC covering a nearly full azimuthal range and large pseodorapidity [34]. A diagram of ATLAS sub-detectors and its tracking detectors is shown in Fig. 6. Details on some systems those are relevant for this analysis will be covered in the following sections.

A right-handed coordinate system with origin located at the nominal interaction point (IP) is used for ATLAS measurements with z-axis being the beam direction. A cylindrical coordinate system (r, ϕ) is defined in the x-y plane, or the *transverse plane*, as shown in Fig. 6. The angle with respect to the beam direction angle is written in terms of pseudorapidity

117 $\eta = -\ln \tan(\theta/2)$, where θ is the polar angle. The measurement of angular separation is
118 written in terms of $\Delta R = \sqrt{(\Delta\eta)^2 + (\Delta\phi)^2}$ between two measured objects [34]. ATLAS
119 data is measured in structure of *events*, and one event is each time the two counter-rotating
120 beams of particles collide at the interaction point [34]. The trigger and data acquisition
121 (TDAQ) systems of ATLAS are used to selectively trigger and save only events of interest
122 [36]. During Run 2, data has been taken for Pb+Pb collisions at $\sqrt{s_{NN}} = 5.02$ TeV, with
123 an integrated recorded luminosity of 0.48 nb^{-1} in 2015 and 1.76 nb^{-1} in 2018 [37].

124   The inner detectors (ID) cover $|\eta| < 2.5$ and are responsible for measuring the trajectory
125 and momentum of charged particles [38]. Located closest to the interaction point, it com-
126 prises of three subsystems of cylindrically coaxial layers that are immersed in a 2 T axial
127 magnetic field. Hits made by charged particles on the inner detectors are clustered and
128 reconstructed as the particle trajectories into objects termed *tracks* [39]. The reconstructed
129 tracks are also used to fit the nuclei interaction point, or primary vertex (PV), in each event,
130 and only one primary vertex is considered in each heavy-ion event. The emitting direction
131 of each track is written in terms of (η, ϕ). Their longitudinal and transverse impact parame-
132 ters $z_0\sin\theta$ and d_0 are also calculated with respect to the primary vertex to help determining
133 whether they come from primary interactions or secondary decays.

134   The calorimeter system measures energy deposit made by particles as they meet and
135 lose their energy to the detectors. In ATLAS, event *centrality* is measured by the total
136 energy deposited ΣE_T in the forward calorimeter (FCal), which covers pseudorapidity range
137 $3.2 < |\eta| < 4.9$. Centrality is closely correlated with the impact parameter of two colliding
138 nuclei [40]. It is defined as a percentile of ΣE_T distribution, starting at 0% for the most
139 central collisions, where two nuclei collide with each other head-on, and increasing to more
140 peripheral collisions with larger impact parameter. Jets in ATLAS heavy-ion collisions are
141 reconstructed from energy deposits in calorimeter towers with the *anti-k_T* algorithm [41].
142 In this algorithm, objects are iteratively clustered into cones of given radius in a procedure
143 that favors clustering a soft particle to its nearby hard particles over nearby soft particles,
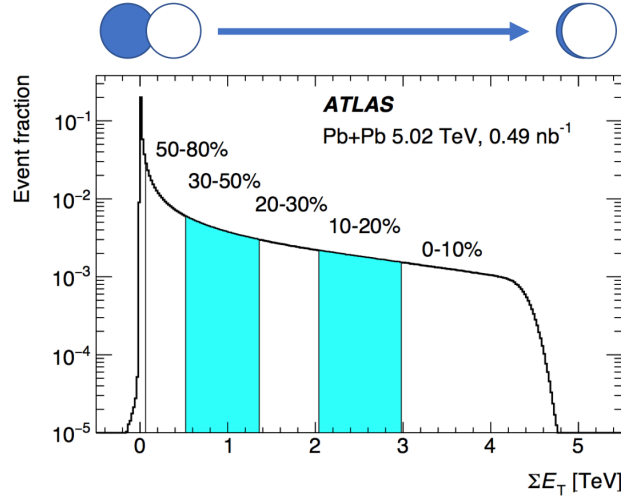144 which defines jet angular direction that's resistant to soft fluctuations.

FIG. 7: ΣE_T distribution for Pb+Pb data at $\sqrt{s_{NN}} = 5.02$ TeV with centrality labelled.

C. Flavor Tagging in Heavy-Ion Collisions and the ATLAS Qualification Task

Flavor tagging is the identification of jets originating from b- and c- quarks [42]. A set of algorithms exploiting the characteristics of the longer lived B- and D- meson decay are developed in pp analysis to identify b- and c- jets from light-flavored jets, using profiles of physics variables extracted from tracks associated to jets. However, these algorithms have not been optimized for heavy ion events, which have a higher occupancy and more *underlying events* (UE), the detector measurements of particles from soft interactions. As shown in Fig. 8a [43], the measured event multiplicity, shown as the measured charged particles N_{ch}, for PbPb is multiple orders of magnitude higher than pp. As a result, more tracks that are not related to jets are used by the algorithm, modifying the physics variables and interfering with tagging.

For my ATLAS authorship qualification task, I studies strategies to optimize the flavor tagging in the heavy ion environment. One approach is to improve the performance of secondary vertex (SV) reconstruction using tracks [44, 45]. SV are reconstructed vertex where heavy flavor hadrons decay. Due to different track distribution in jets between PbPb and pp jets, I found that the spatial proximity based track-to-jet association algorithm "shrinking cone" [46] was tuned based on pp simulations, thus excluding useful tracks for PbPb samples. On the other hand, UE and fake tracks are dominantly low p_T, as shown in Fig. 8b, the spectrum of UE and fake tracks quickly drop with p_T [31]. Consequently, the high fake rate as shown in Figure 9a can be decreased by choosing a higher p_T cut on
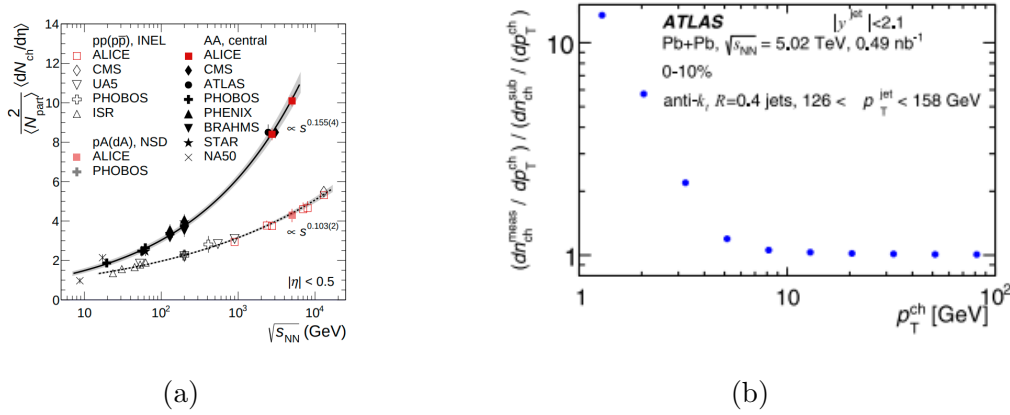
(a)   (b)

FIG. 8: (left) Event multiplicity at different system [43] and (right) ratio of measured charged-particle distribution before and after background subtraction in ATLAS [31].

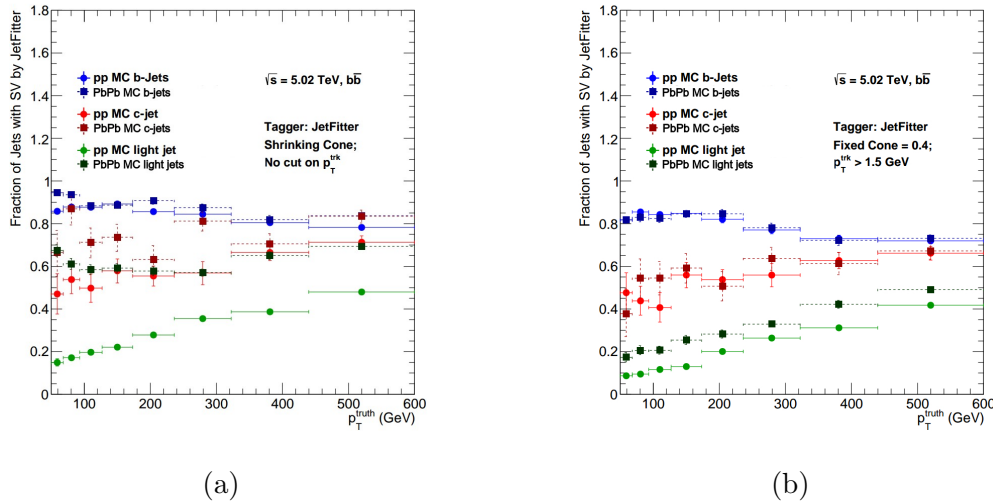(a)   (b)

FIG. 9: The secondary vertexing performance using the tagger JetFitter [44] with (left) the shrinking cone track-to-jet association and no requirements on track minimum p_T, and (right) shows results with fixed cone at $R = 0.4$ and tracks with $p_T > 1.5$ GeV. Solid lines are for pp for reference, dashed lines are for PbPb.

tracks. The combination of these two strategies are shown to reduce fake rate significantly without impact vertexing efficiency significantly, as shown in 9b.

To reduce the effect of centrality dependence, I also remade templates of the track impact parameters with PbPb simulations for each centrality bin, and tag samples from the same centrality. As shown in Fig. 10, the tagging receiver operating characteristic (ROC) curve
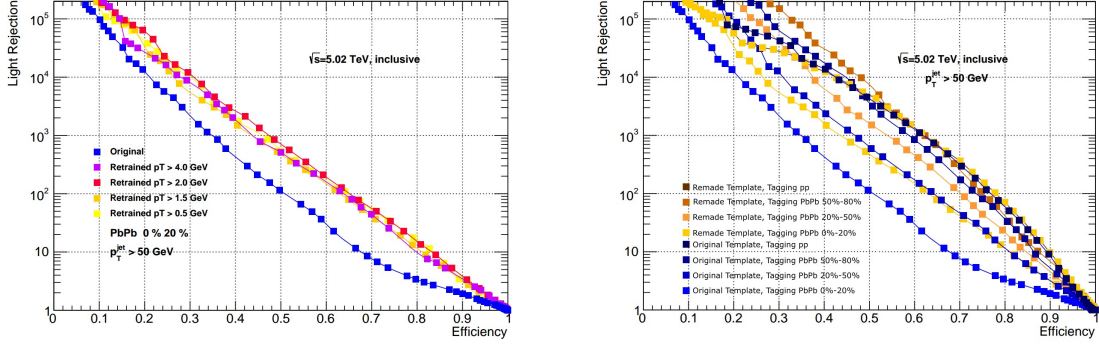
FIG. 10: ROC cruve for tagging using IP3D, the impact parameter tagger, with pp template and templates remade from centrality-binned $PbPb$ simulations with different p_T selections for, (left) most central events and (right) all centrality bins.

plotting inverse of fake rate (light rejection) versus tagging efficiency using remade templates are improved and has a weaker centrality dependence.

III.   ANALYSIS TECHNIQUE

The method of multi-particle cumulants decomposes the correlations between all particles in an event into the sum of terms involving correlations between smaller number of particles. In the standard cumulant method [47, 48], The event-averaged azimuthal correlations between two- and four-particle are defined as,

$$\langle\langle 2 \rangle\rangle \equiv \langle\langle e^{in(\phi_1-\phi_2)} \rangle\rangle = \frac{\sum_i^{events}(W_{(2)})_i \langle 2 \rangle_i}{\sum_i^{events}(W_{(2)})_i} \tag{3}$$

$$\langle\langle 4 \rangle\rangle \equiv \langle\langle e^{in(\phi_1+\phi_2-\phi_3-\phi_4)} \rangle\rangle = \frac{\sum_i^{events}(W_{(4)})_i \langle 2 \rangle_i}{\sum_i^{events}(W_{(4)})_i} \tag{4}$$

where $\langle n \rangle_i$ is the single-event n-particle correlations for event i. The second order cumulant $c_n\{2\}$ is defined as,

$$c_n\{2\} \equiv \langle\langle e^{in(\phi_1-\phi_2)} \rangle\rangle - \langle e^{in\phi_1} \rangle \langle e^{-in\phi_2} \rangle = \langle\langle 2 \rangle\rangle - \langle\langle 1 \rangle\rangle^2 \tag{5}$$

And the second term vanishes when detector acceptance is uniform. For uniform detectors, the fourth-order cumulant $c_n\{4\}$ is defined as,

$$c_n\{4\} = \langle\langle 4 \rangle\rangle - 2\langle\langle 2 \rangle\rangle^2 \tag{6}$$

184 These cumulants are averaged over all particles, and they reflect the integrated flow terms
185 by these relations,

$$c_n\{2\} = \langle\langle v_n^2 \rangle\rangle,$$
$$c_n\{4\} = \langle\langle v_n^4 \rangle\rangle - 2\langle\langle v_n^2 \rangle\rangle^2 \tag{7}$$

186 The ratio of cumulants reveals distributions of measured v_n. For example, since the
187 variance of v_n^2, $\sigma^2(v_n^2) \equiv \langle v_2^4 \rangle - \langle v_2^2 \rangle^2$,

$$\left(\frac{v_2\{4\}}{v_2\{2\}}\right)^4 = 2 - \frac{\langle v_2^4 \rangle}{\langle v_2^2 \rangle^2} = 1 - \frac{\sigma^2(v_n^2)}{\langle v_2^2 \rangle^2} \tag{8}$$

188 It can be derived, as shown in Ref [49], for Bessel-Gaussian or elliptic power v_2 distribu-
189 tion, $v_2\{4\} \approx v_2\{6\} \approx v_2\{8\}$. An observation of this pattern at high p_T region will therefore
190 suggests a correlation between high p_T anisotropy and event-by-event fluctuations [49].

191 The experimental measurement of p_T dependent differential flow harmonics $v_n(p_T)$ in the
192 statistically limited high p_T region is usually carried out utilizing a correlator of one hard
193 particle in given p_T range to one or more soft particles with no p_T requirement. Denoting the
194 single-event k-particle correlation as $\langle k' \rangle$, the differential cumulants $d_n\{2\}(p_T)$, $d_n\{4\}(p_T)$
195 and different flow $v_n\{4\}(p_T)$, $v_n\{4\}(p_T)$ are derived by Ref. [47, 48] to be,

$$d_n\{2\}(p_T) = \langle\langle 2' \rangle\rangle,$$
$$d_n\{4\}(p_T) = \langle\langle 4' \rangle\rangle - 2\langle\langle 2' \rangle\rangle\langle\langle 2 \rangle\rangle \tag{9}$$

$$v_n\{2\}(p_T) = \frac{d_n\{2\}(p_T)}{(c_n\{2\})^{1/2}},$$
$$v_n\{4\}(p_T) = \frac{d_n\{4\}(p_T)}{(-c_n\{4\})^{3/4}} \tag{10}$$

196 The event-averaged differential correlators $\langle\langle k' \rangle\rangle$ can be computed with equation (3) and (4)
197 by replacing $\langle k \rangle$ with its differential variant $\langle k' \rangle$. An event weight is chosen to minimize the
198 effect of event multiplicity. Experimentally, the event weight W_i is the number of different
199 k-particle combinations in that event [48].

200 It has been shown in Ref [25] that, if the fluctuations of high p_T v_2 were correlated to the
201 soft fluctuations exactly in a linear manner, then, $v_2\{4\}(p_T)/v_2\{2\}(p_T) = v_2\{4\}/v_2\{2\}$ for
202 all p_T. Meanwhile, the difference between fluctuations in soft and in hard sector, $\Delta_n^{SH}(p_T)$
203 can be obtained using,

$$\Delta_n^{SH}(p_T) \equiv \left(\frac{v_n\{2\}}{v_n\{4\}}\right)^5 \left[\frac{v_n\{4\}(p_T)}{v_n\{2\}(p_T)} - \frac{v_n\{4\}}{v_n\{2\}}\right] \tag{11}$$

IV. PROPOSED RESEARCH

The geometry of QGP is converted into azimuthal anisotropy in final state particles in low p_T region. The efficiency of this conversion depends on transport properties of the QGP, which can be modelled with a nearly ideal relativistic fluid. The event-by-event fluctuations of nucleon positions leads to the measured third and higher order flow harmonics. Hard-scattered partons interact with and lose energy to the QGP. This has been measured by "jet quenching" observables such as nuclear modification factor R_{AA}. The energy loss depends distance travelled in the medium and thus the azimuthal direction, creating high p_T anisotropy.

The role of fluctuations in high p_T anisotropy needs deeper understanding. If hard-scattered particle responses linearly to initial geometry fluctuations, why is high p_T v_3 measured consistent with zero? What are the effects of fluctuations in parton energy loss and jet fragmentation? To understand this, we propose to measure the high p_T differential flow using multi-particle cumulant methods with charged particles as high as statistics permits with the 1.76 μb^{-1} of $\sqrt{s_{NN}} = 5.02$ TeV PbPb ATLAS data in 2018. The ratio for integrated flow $v_2\{4\}/v_2\{2\}$ is sensitive to the fluctuations in v_2, and the ratio of differential flow $v_2\{4\}(p_T)/v_2\{2\}(p_T)$ is sensitive to the high p_T response to low p_T quantities. The combination of the two variables defines $\Delta_{SH}(p_T)$ that separates soft sector fluctuations from those in hard sector. Modelling of these quantities using LHC condition for $\sqrt{s_{NN}} = 5.02$ Tev PbPb collision is also available for comparison [25].

The proposed timeline is as follow. Firstly, the performance of tracks should be evaluated, including the momentum resolution of tracks, trigger efficiency and track reconstruction efficiency. This should take approximately 3 months. Then, correction strategies should be developed, exploiting techniques developed by previous ATLAS and other LHC anisotropy measurements. The completion of these corrections will prepare for a preliminary measurements with uncertainties evaluated, and we plan to have this preliminary result by the Spring of 2022, with the finalization and documentation of results by the Fall of 2022.

---

[1] M. Thomson, *Modern particle physics* (Cambridge University Press, New York, 2013).

[2] P. F. Kolb and U. W. Heinz, (2003), arXiv:nucl-th/0305084.

[3] A. M. Poskanzer and S. A. Voloshin, Phys. Rev. C **58**, 1671 (1998), arXiv:nucl-ex/9805001.

[4] M. S. H.Zbroszczyk, in *Proc. of 5th International Conference on New Frontiers in Physics*, EPJ Web Conf. (EDP Sciences, 2017) p. 8.

[5] L. D. Landau, Izv. Akad. Nauk Ser. Fiz. **17**, 51 (1953).

[6] U. W. Heinz and P. F. Kolb, Nucl. Phys. A **702**, 269 (2002), arXiv:hep-ph/0111075.

[7] H. Petersen, J. Phys. G **41**, 124005 (2014), arXiv:1404.1763 [nucl-th].

[8] B. Alver and G. Roland, Phys. Rev. C **81**, 054905 (2010), [Erratum: Phys.Rev.C 82, 039903 (2010)], arXiv:1003.0194 [nucl-th].

[9] S. A. Voloshin, A. M. Poskanzer, and R. Snellings, Landolt-Bornstein **23**, 293 (2010), arXiv:0809.2949 [nucl-ex].

[10] B. Schenke, C. Shen, and P. Tribedy, Phys. Rev. C **102**, 044905 (2020), arXiv:2005.14682 [nucl-th].

[11] H. Niemi, K. J. Eskola, and R. Paatelainen, Phys. Rev. C **93**, 024907 (2016), arXiv:1505.02677 [hep-ph].

[12] (2015).

[13] G. Aad *et al.* (ATLAS), Eur. Phys. J. C **73**, 2509 (2013), arXiv:1304.4739 [hep-ex].

[14] G. Aad *et al.* (ATLAS), Eur. Phys. J. C **71**, 1512 (2011), arXiv:1009.5908 [hep-ex].

[15] M. Aaboud *et al.* (ATLAS), JHEP **09**, 020, arXiv:1706.03192 [hep-ex].

[16] V. Khachatryan *et al.* (CMS), Eur. Phys. J. C **76**, 451 (2016), arXiv:1605.04436 [hep-ex].

[17] M. Aaboud *et al.* (ATLAS), JHEP **05**, 195, arXiv:1711.02692 [hep-ex].

[18] Z. Nagy, Phys. Rev. Lett. **88**, 122003 (2002), arXiv:hep-ph/0110315.

[19] M. Aaboud *et al.* (ATLAS), Phys. Lett. B **790**, 108 (2019), arXiv:1805.05635 [nucl-ex].

[20] X.-N. Wang, Phys. Rev. C **63**, 054902 (2001), arXiv:nucl-th/0009019.

[21] B. Abelev *et al.* (ALICE), JHEP **03**, 013, arXiv:1311.0633 [nucl-ex].

[22] G. Aad *et al.* (ATLAS), JHEP **09**, 050, arXiv:1504.04337 [hep-ex].

[23] A. A. Baty (CMS), Nucl. Part. Phys. Proc. **289-290**, 421 (2017).

[24] S. Chatrchyan *et al.* (CMS), Eur. Phys. J. C **72**, 1945 (2012), arXiv:1202.2554 [nucl-ex].

[25] J. Noronha-Hostler, B. Betz, M. Gyulassy, M. Luzum, J. Noronha, I. Portillo, and C. Ratti 10.1103/PhysRevC.95.044901 (2016), arXiv:1609.05171.

[26] W. Zhao, W. Ke, W. Chen, T. Luo, and X.-N. Wang, (2021), arXiv:2103.14657 [hep-ph].

[27] A. M. Sirunyan *et al.*, Phys. Lett. B **776**, 195 (2018), arXiv:1702.00630.

[28] ATLAS-CONF-2020-019 (ATLAS), (2020), https://cds.cern.ch/record/2720249.

[29] J. Adam *et al.* (ALICE), Phys. Lett. B **753**, 511 (2016), arXiv:1509.07334 [nucl-ex].

[30] G. Aad *et al.* (ATLAS), Phys. Rev. Lett. **111**, 152301 (2013), arXiv:1306.6469 [hep-ex].

[31] M. Aaboud *et al.* (ATLAS), Phys. Rev. C **98**, 024908 (2018), arXiv:1805.05424 [nucl-ex].

[32] B. Betz and M. Gyulassy, JHEP **08**, 090, [Erratum: JHEP 10, 043 (2014)], arXiv:1404.6378 [hep-ph].

[33] JINST **3**, S08001.

[34] T. A. C. et.al, Journal of Instrumentation **3** (08), S08003.

[35] F. Kuger, *Signal Formation Processes in Micromegas Detectors and Quality Control for large size Detector Construction for the ATLAS New Small Wheel*, Ph.D. thesis, U. Wurzburg (main) (2017), arXiv:1708.01624 [physics.ins-det].

[36] S. Ballestrero, W. Vandelli, and G. Avolio (ATLAS TDAQ), Phys. Procedia **37**, 1819 (2012).

[37] G. Aad *et al.* (ATLAS), Eur. Phys. J. C **80**, 47 (2020), arXiv:1909.00761 [hep-ex].

[38] G. Aad *et al.* (ATLAS), Eur. Phys. J. C **80**, 1194 (2020), arXiv:2007.07624 [hep-ex].

[39] G. Aad *et al.* (ATLAS), JHEP **09**, 050, arXiv:1504.04337 [hep-ex].

[40] G. Aad *et al.* (ATLAS), Phys. Lett. B **710**, 363 (2012), arXiv:1108.6027 [hep-ex].

[41] M. Cacciari, G. P. Salam, and G. Soyez 10.1088/1126-6708/2008/04/063 (2008), arXiv:0802.1189.

[42] G. Aad *et al.* (ATLAS), Eur. Phys. J. C **79**, 970 (2019), arXiv:1907.05120 [hep-ex].

[43] J. Adam *et al.* (ALICE), Phys. Lett. B **772**, 567 (2017), arXiv:1612.08966 [nucl-ex].

[44] G. Piacquadio and C. Weiser, J. Phys. Conf. Ser. **119**, 032032 (2008).

[45] V. Kostyukhin, (2003), https://cds.cern.ch/record/685551/.

[46] ATL-PHYS-PUB-2017-010 (ATLAS), (2017), https://cds.cern.ch/record/2268678.

[47] N. Borghini, P. M. Dinh, and J.-Y. Ollitrault, Phys. Rev. C **64**, 054901 (2001), arXiv:nucl-th/0105040.

[48] A. Bilandzic, R. Snellings, and S. Voloshin, Phys. Rev. C **83**, 044913 (2011), arXiv:1010.0233 [nucl-ex].

[49] L. Yan, J.-Y. Ollitrault, and A. M. Poskanzer, Phys. Lett. B **742**, 290 (2015), arXiv:1408.0921 [nucl-th].